Journal of Alloys and Compounds 1010 (2025) 177205

Contents lists available at ScienceDirect

Journal of Alloys and Compounds

journal homepage: www.elsevier.com/locate/jalcom

Synthesis, magnetic and structural properties of (1-x)$LiFe_5O_8$–(x) $LiZn_{2.5}Ti_{2.5}O_8$ spinel solid solutions

A.A. Zabolotnyi[a], A.V. Motseyko[a], S.P. Kubrin[a], A.S. Komlev[b], S.A. Guda[c], Yu.V. Rusalev[c], A.V. Nazarenko[d], N.V. Ter-Oganessian[a,*,1]

[a] Institute of Physics, Southern Federal University, Rostov-on-Don 344090, Russia
[b] Faculty of Physics, Lomonosov Moscow State University, Moscow 119991, Russia
[c] The Smart Materials Research Institute, Southern Federal University, Rostov-on-Don 344090, Russia
[d] Southern Scientific Center of the Russian Academy of Sciences, Rostov-on-Don 344006, Russia

ARTICLE INFO

Keywords:
Spinel
$LiFe_5O_8$
Magnetic properties
Atomic ordering
Monte Carlo calculations

ABSTRACT

Compounds with the spinel structure present a technologically important class of materials. Spinels show a great variety of magnetic and magnetoelectric phenomena owing to the facile entrance of transition metals in the cationic sublattices. One of such examples is lithium ferrite $LiFe_5O_8$ with high ferrimagnetic phase transition temperature and cationic order-disorder transformations. The latter are important as they influence the crystal symmetry, which is crucial for physical properties. In this work we synthesize a series of (1-x)$LiFe_5O_8$–(x)$LiZn_{2.5}Ti_{2.5}O_8$ ($0 \leq x \leq 1$) solid solutions and characterize them with various experimental and theoretical methods. The solid solutions experience a series of concentrational phase transformations between atomically ordered ($P4_{3(1)}32$) and disordered ($Fd\bar{3}m$) phases. The variation with concetration x of Fe^{3+} occupancies in cationic sublattices is studied using Mössbauer spectroscopy. The Mössbauer and magnetic measurements reveal sharp suppression of magnetic properties at $x \geq 0.5$ when the number of Fe^{3+} ions in the A-sublattice vanishes. The magnetic behaviour in the studied series of solid solutions is confirmed by Monte Carlo calculations with magnetic exchange interactions determined using the density functional theory.

1. Introduction

Rapid development of microelectronics, information and wireless technologies require new multifunctional materials with both high reliability and a wide range of magnetic and electrical properties. Among such materials, chemical compounds with the spinel structure are of high scientific interest. They are used as high-speed ferrite modulators and phase shifters, some compounds are used in memory devices, in computer technology, as electrode materials in Li-ion batteries, etc [1–6].

The oxide spinel with the general chemical formula AB_2O_4 has a face-centered cubic crystal structure described by the space group $Fd\bar{3}m$ (O_h^7). The tetrahedrally coordinated A-cations form the diamond lattice, whereas the octahedrally coordinated B-cations form the pyrochlore lattice. The variety of spinel compounds exhibiting different properties is due to the easy substitution of metal ions into cationic sublattices. In the case of the presence of transition metals, the competition between magnetic spin exchange interactions inside or between the diamond and pyrochlore cationic sublattices often results in complex magnetic phenomena. Furthermore, these two sublattice types themselves are prone to frustration of magnetic interactions, which adds to the complexity of magnetism in spinels.

The diversity of magnetic properties and types of emerging magnetic order in spinels makes this crystal class useful for the search for compounds that are multiferroic or exhibit a linear magnetoelectric (ME) effect. Despite this variety of magnetic spinels, a relatively small number of multiferroics or magnetoelectrics have been discovered to date [7]. A necessary condition for the emergence of a non-trivial magnetoelectric coupling is the suppression of the inversion center of the crystal structure. In spinels, the presence of different kinds of atoms in cationic

---

* Corresponding author.
E-mail addresses: zabolotnyi@sfedu.ru (A.A. Zabolotnyi), moceyko@sfedu.ru (A.V. Motseyko), spkubrin@sfedu.ru (S.P. Kubrin), alkomlev98@yandex.ru (A.S. Komlev), gudasergey@sfedu.ru (S.A. Guda), rusalev@sfedu.ru (Yu.V. Rusalev), avnazarenko1@gmail.com (A.V. Nazarenko), teroganesyan@sfedu.ru (N.V. Ter-Oganessian).
[1] 0000–0001-8965–1800

https://doi.org/10.1016/j.jallcom.2024.177205
Received 17 July 2024; Received in revised form 9 September 2024; Accepted 21 October 2024
Available online 23 October 2024
0925-8388/© 2024 Elsevier B.V. All rights reserved, including those for text and data mining, AI training, and similar technologies.

sublattices leads to the possibility of atomic ordering, which can suppress the center of inversion. One of the possibilities is the 1:1 at. ordering in the *A*-sublattice. The examples of spinels exhibiting such atomic ordering in the *A*-sublattice are $Li_{1/2}Ga_{1/2}Cr_2O_4$, $Li_{1/2}In_{1/2}Cr_2O_4$ [8], $Cu_{1/2}In_{1/2}Cr_2S_4$ [9], and $Fe_{1/2}Cu_{1/2}Cr_2S_4$ [10,11]. It results in reduction of the crystal symmetry to noncentrosymmetric $F\overline{4}3$ m, which may allow for linear ME effect or facile appearance of multiferroic properties [12].

One of the representatives of interesting magnetic spinels exhibiting atomic order-disorder phenomena is lithium ferrite $LiFe_5O_8$. It attracts attention of researchers as the basis component for perspective materials due to its high saturation magnetization value, mixed type of conductivity, high magnetic Curie temperature ($\sim$ 900 K), as well as due to its promising potential for use in Li-ion batteries [4,13]. A feature of the structure of $LiFe_5O_8$ is the presence of two crystallographic phases: an ordered α-$LiFe_5O_8$ (sp. gr. $P4_{3(1)}32$) and a disordered β-$LiFe_5O_8$ (sp. gr. $Fd\overline{3}m$). The reversible phase transition between these phases is observed at $1008 - 1028$ K [14,15]. In the first case, the 1:3-type atomic ordering of Li^+ and Fe^{3+} in the *B*-sublattice is observed. The α-$LiFe_5O_8$ phase has a cubic unit cell parameter $a = 8.3339$ Å, while the β-$LiFe_5O_8$ phase cell parameter is slightly larger $a = 8.3409$ Å [16].

Despite the fact that the ordered crystal structure lacks the inversion symmetry, it admits only a higher order ME effect [7,17,18], which is the consequence of the space group symmetry. In [19] it is claimed that unlike many other oxide spinels, which have been shown to exhibit the ME effect at relatively low temperatures (usually below 30 K), $LiFe_5O_8$ demonstrates a decent ME effect at much higher temperatures with a maximum ME coefficient reaching $2\ mV \cdot Oe^{-1} \cdot cm^{-1}$ at temperatures up to 120 K. It is considered that Fe^{3+} ions residing at non-centrosymmetric sites together with the atomic ordering lead to a coupling between local electric dipole moments and spins through the spin-orbit interaction, leading to the observed magnetoelectricity in $LiFe_5O_8$.

Cationic substitution in $LiFe_5O_8$ allows tuning its properties. For example, when Zn^{2+} is introduced into $LiFe_5O_8$ the saturation magnetization increases, which opens up prospects for broad application in microwave technology [20–23]. In turn, the substitution of Ti for Fe leads to a monotonous decrease in saturation magnetization [24]. Spinels simultaneously containing Li^+, Fe^{3+}, Zn^{2+}, and Ti^{4+} ions were reported [25–28], however they contain varying amounts of Li atoms. In Li-containing $LiMCr_4O_8$ (M = Ga, Fe, In) spinels the Li atoms occupy half of the *A*-sublattice sites, which results in 1:1 at. ordering of Li^+ and M^{3+} in the *A*-sublattice [29–31]. Such atomic ordering leads to the noncentrosymmetric $F\overline{4}3$ m crystal structure that allows linear ME effect [12], which however was not confirmed in these spinels possibly due to the special types of appearing magnetic order [7]. Therefore, it might be reasonable to simultaneously substitute Zn^{2+} and Ti^{4+} ions in $LiFe_5O_8$ for Fe^{3+} ions, without changing the amount of Li^+ with the aim of obtaining similar atomic ordering in the *A*-sublattice of these solid solutions.

Therefore, in this work a series of solid solutions (1-x)$LiFe_5O_8$–(x)$LiZn_{2.5}Ti_{2.5}O_8$ ($0 \le x \le 1$) were synthesized by a high-temperature solid-phase method. The crystal structure of the obtained compounds was studied by full-profile analysis using the Rietveld algorithm. Magnetic ordering temperatures and the local crystalline environment of iron were studied by Mössbauer spectroscopy. Magnetic hysteresis loops were studied at room temperature, and the temperature dependence of magnetization was measured. We determined the magnetic exchange constants for $LiFe_5O_8$ with the help of density functional theory calculations and used them in Monte Carlo studies of magnetic properties for the whole concentrational range of the solid solutions.

2. Experimental methods

The solid solutions (1-x)$LiFe_5O_8$–(x)$LiZn_{2.5}Ti_{2.5}O_8$ ($0 \le x \le 1$) (LFZT) with concentration x varied in steps of 0.1 were synthesized by a high-temperature solid-phase method. We used Li_2CO_3 (99.9 %), α-Fe_2O_3 (99.7 %), ZnO (99.5 %) and TiO_2 (99.9 %) as initial reagents and the reaction scheme can be written as

$$\frac{1}{2}Li_2CO_3 + \frac{5x}{2}TiO_2 + \frac{5-5x}{2}Fe_2O_3 + \frac{5x}{2}ZnO \longrightarrow LiZn_{2.5x}Fe_{(5-5x)}Ti_{2.5x}O_8. \quad (1)$$

The powders of the initial reagents were thoroughly crushed and mixed in an agate mortar with the addition of ethyl alcohol (95 %) for 30 min. The obtained mixture was calcined in a corundum crucible in air at a temperature of 900 ˚C for 6 h, the heating rate was 3 ˚C/min. After that, the samples were cooled to room temperature at the rate of cooling of the furnace. The obtained powders were homogenized again with the addition of polyvinyl alcohol (5 %) in an agate mortar for 30 min, after which they were pressed into discs with a diameter of 10 mm at a pressure of 50 bar and calcined at a temperature of 1000 ˚C for 4 h; the heating speed was 3 ˚C/min. At 1000 ˚C, the formation of a pure phase for compositions $x = 0$, 0.1, 0.2, 0.3, and 1 was confirmed by the XRD method. For the remaining samples, the obtained discs were crushed, pressed, and calcined again with the repetition of all conditions, only the final temperature for compositions $x = 0.4$ and 0.9 was 1050 ˚C, and for $x = 0.5$, 0.6, 0.7, and 0.8 it was 1100 ˚C.

The powder X-ray data were collected using the DRON-3M diffractometer with an installed Fe-filter of Co Kα radiation at a rate of 2˚ (2θ)/min. The Match program with the PDF-2 database (ICCD) was used for phase analysis.

To refine the crystal structure by the Rietveld method, the X-ray diffraction data in the angle range $15^\circ \le 2\theta \le 120^\circ$ with the step of 0.03˚ and an exposure at each point of 3 s was used. The data obtained was analyzed in the FULLPROF [32] program using the WinPLOTR graphical interface [33]. The crystal structures of α-$LiFe_5O_8$ (sp. gr. $P4_{3(1)}32$) [34] and β-$LiFe_5O_8$ (sp. gr. Fd-3m) [35] were taken as the initial models to clarify the crystal structure of the obtained compounds.

The Mössbauer spectra were measured using the MS1104Em spectrometer. ^{57}Co in the Rh matrix was used as a source of gamma quanta. For cooling, the samples were placed in the chamber of the CCS-850 cryostat. The model interpretation of the spectra was performed using the SpectrRelax [36] software. Isomer shifts were calculated relative to the spectrum of metallic α-Fe measured at room temperature.

The microstructure of the obtained samples was studied on pre-ground ceramic samples at the Center for Shared Use of the Southern Scientific Center of the Russian Academy of Sciences (https://ckprf.ru/catalog/ckp/501994/) using the scanning electron microscope (SEM) Carl Zeiss EVO 40. The SEM analysis was carried out under high accelerating voltage and low probe current with acquisition conditions of EHT = 20 kV, I_{probe} = 20 pA, and $8 - 9$ mm working distance.

Room temperature magnetic measurements were carried out on a VSM Lakeshore 7404 magnetometer. The magnetization $M(H)$ curves were measured in the field range $-$ 17–17 kOe. For each measurement there are at least 160 points with 10 s measurement time per point. Temperature-dependent magnetic measurements were carried out with VSM LakeShore 7407 Series. The heating and cooling rates during the magnetization measurement were 2 K/min. The sample was fixed to the holder using Zircar Cement during measurements in the oven.

To determine the magnetic exchange constants in the studied solid solutions we performed spin-polarized density functional theory (DFT) calculations using the Vienna *Ab-initio* Simulation Package (VASP) [37] and the projected augmented wave method [38]. We used the generalized gradient approximation (GGA) of exchange correlation based on the Perdew-Burke-Ernzerhof functional [39], which was corrected by means of the GGA+U formalism for the Fe atoms with $U_{eff} = U - J = 3$ eV within the Dudarev approach [40]. The energy cutoff was 500 eV and the Brillouin zone integration was done using the set of $6 \times 6 \times 6$ points for the cubic spinel unit cell. The magnetic exchange constants were

Table 1
Magnetic exchange constants for $LiFe_5O_8$.

	J_{BB}	$J_{AB}^{(1)}$	$J_{AB}^{(2)}$	$J_{AB}^{(3)}$	$J_{AA}^{(1)}$	$J_{AA}^{(2)}$
d, Å	2.99	3.39	3.45	3.51	3.59	3.66
J, meV	8.9	61.7	52.5	37.6	4.4	4.4

determined for the nearest neighbour $A-A$, $A-B$, and $B-B$ inter- and intrasublattice interactions for the $LiFe_5O_8$ compound using the following procedure. To determine the exchange constant between two spins at a certain distance, we calculated the energies of four spin configurations: two up (↑↑), two down (↓↓), and one up one down (↑↓ and ↓↑), keeping the directions of all other spins according to the ferrimagnetic arrangement, i.e., spins up for Fe in octahedral environment and spins down for Fe at tetrahedral sites. The combinations of respective energies $E_{\uparrow\uparrow}+E_{\downarrow\downarrow}-E_{\uparrow\downarrow}-E_{\downarrow\uparrow}$ can be expressed through the exchange constants in the Heisenberg Hamiltonian

$$\mathscr{H}=\sum_{ij}J_{ij}\vec{S}_i\cdot\vec{S}_j, \tag{2}$$

where $\vec{S}$ are classical vectors of unit length. This either directly gives the sought-for exchange constant without any contribution from other exchange paths, or allows for its easy calculation from a system of linear equations. The resulting exchange constants are given in Table 1. The distances are given with respect to the ordered spinel structure with the cubic unit cell value $a = 8.3339$ Å shown in Fig. 1(a). Figs. 1(b,c,d) visualize the magnetic exchange paths used in the present work. In the case when the disordered crystal structure is modeled using the Monte Carlo method described below and the Fe^{3+} ions enter into the former Li^+ sublattice, the exchange constants between their spins and other Fe^{3+} spins are taken as the average of similar J values. Fig. 1 has been created using the VESTA software [41].

The obtained magnetic exchange constants are further employed in classical Monte Carlo (MC) calculations of the Heisenberg Hamiltonian Eq. (2) using the Metropolis scheme. The size of the simulation box was $22\times22\times22$ cubic unit cells with periodic boundary conditions, which ensured independence of the results on the simulation box size. To model solid solutions we progressively removed spins from the lattice in correspondence with the concentration x of $LiZn_{2.5}Ti_{2.5}O_8$ and assuming either the experimentally determined or uniform distribution of Fe^{3+} ions in both cationic sublattices A and B. The system was monotonously cooled from the paramagnetic state down to 1 K in steps of 1 K. After each change of temperature the system was allowed to relax for 10^3 MC steps per spin (MCS) and the statistical information was subsequently gathered over the next 10^3 MCS.

3. Results and discussion

3.1. Mössbauer spectroscopy

Since the results of Mössbauer spectroscopy are used for interpretation of the X-ray diffraction, we first describe the corresponding data. Fig. 2 shows the Mössbauer spectra of the LFZT solid solution measured at room temperature. The spectra of samples with $0.5\leq x\leq0.9$ represent quadrupole splitting lines. These spectra are described by a single paramagnetic doublet with the values of isomer shift $\delta=0.35\pm0.02$ mm/s and quadrupole splitting $\Delta=0.48\pm0.02$ mm/s. The value of the isomer shift of these doublets is typical for Fe^{3+} ions in oxygen octahedra [42].

The Mössbauer spectra of the samples with $0.1\leq x\leq0.4$ represent broadened Zeeman splitting lines. The distribution functions of hyperfine magnetic field $P(H)$ were used for the model interpretation of these spectra [36]. Isomer shifts δ of $P(H)$ are in the range of values from 0.2 to 0.37 mm/s, which are characteristic of Fe^{3+} ions in both octahedral and tetrahedral oxygen environments [42]. The values of the quadrupole shift ε of the $P(H)$ function range $-$ 0.01–0 mm/s. The $P(H)$ functions for the spectra of samples $0.2\leq x\leq0.4$ have a set of local maxima in the range of values of hyperfine magnetic fields $H=0-500$ kOe. With an increase in x, the intensity of local maxima at $H<400$ kOe increases, while the intensity of the local maximum in the vicinity of $H\approx480$ kOe decreases. The $P(H)$ distribution for the $x=0.1$ sample is in the range H

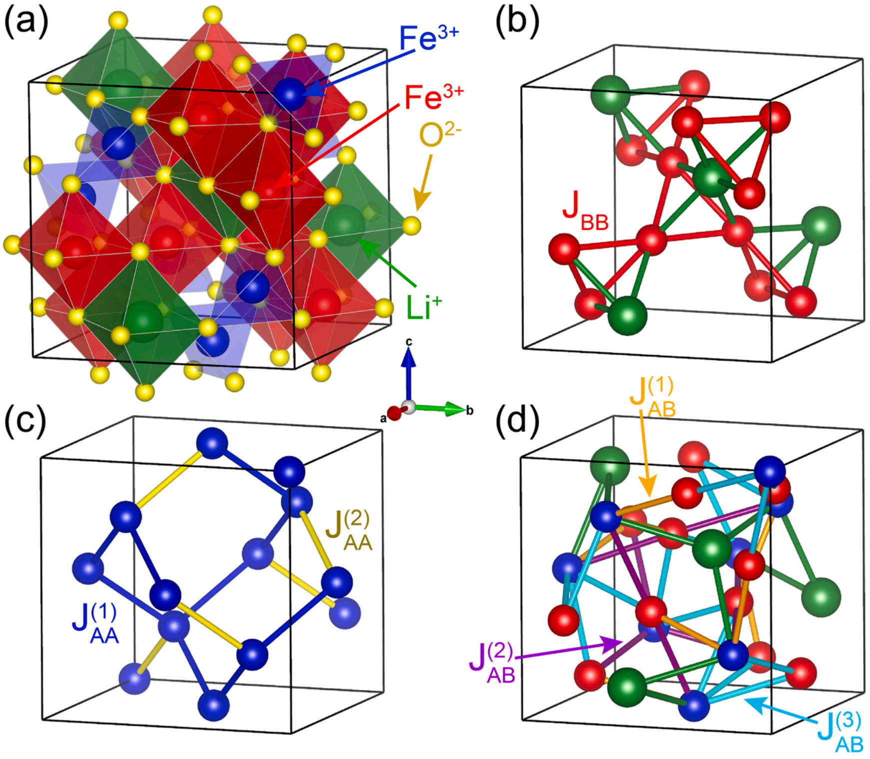

Fig. 1. (a) Ordered cubic unit cell of $LiFe_5O_8$. (b), (c), and (d) give the same unit cell showing the magnetic exchange interactions determined in the present work.

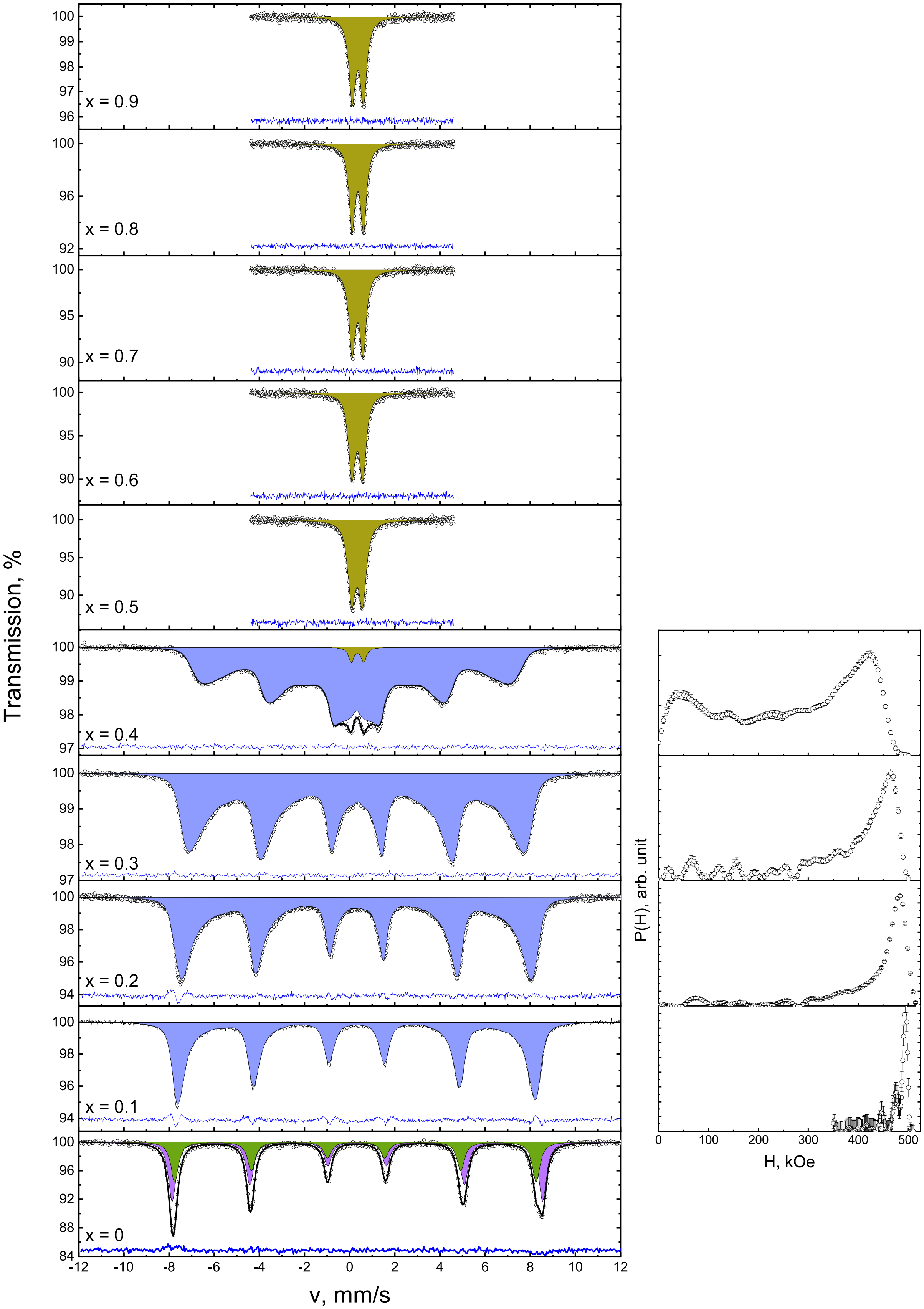

Fig. 2. Mössbauer spectra of the (1-x)$LiFe_5O_8$–(x)$LiZn_{2.5}Ti_{2.5}O_8$ solid solutions taken at 298 K.

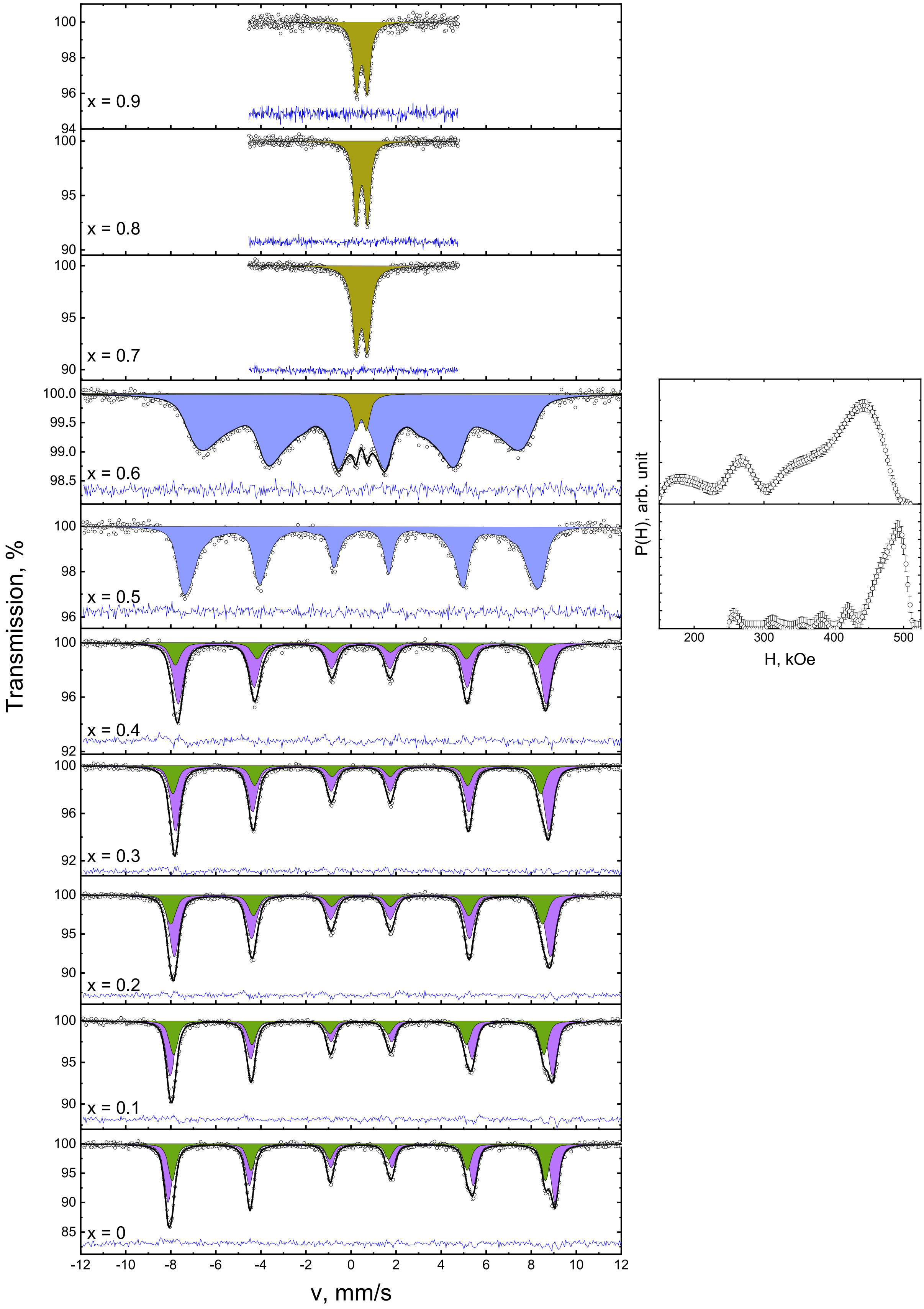

Fig. 3. Mössbauer spectra of the (1-x)$LiFe_5O_8$–(x)$LiZn_{2.5}Ti_{2.5}O_8$ solid solutions taken at 15 K.

Table 2
Parameters of Mössbauer spectra for (1-x)$LiFe_5O_8$–(x)$LiZn_{2.5}Ti_{2.5}O_8$ taken at 15 K. Here δ is the isomer shift, ε is the quadrupole shift, Δ is the quadrupole splitting for paramagnetic component, H is the hyperfine magnetic field on ^{57}Fe nucleus, Γ is the linewidth, and A is the component area.

x	Component	$\delta \pm 0.02$	$\Delta/\varepsilon \pm 0.02$	$H \pm 1$	$\Gamma \pm 0.02$	$A \pm 1$ %
0	S1	0.35	−0.01	514	0.41	39
	S2	0.46	0.01	532	0.41	61
0.1	S1	0.35	−0.01	510	0.48	38
	S2	0.46	0.02	526	0.48	62
0.2	S1	0.35	−0.01	512	0.54	32
	S2	0.46	0.04	518	0.54	68
0.3	S1	0.35	−0.01	507	0.50	30
	S2	0.46	0.03	506	0.50	70
0.4	S1	0.35	−0.01	498	0.56	27
	S2	0.46	0.03	507	0.56	73
0.5	P(H)	0.45	–	491*	0.44	100
0.6	D	0.46	0.46		0.37	5
	P(H)	0.44	–	446*	0.60	95
0.7	D	0.47	0.49		0.40	100
0.8	D	0.48	0.50		0.32	100
0.9	D	0.48	0.48		0.34	100

= 350 − 500 kOe and has a high-intensity local maximum at $H \approx$ 480 kOe and a set of low-intensity local maxima at lower hyperfine fields.

The Mössbauer spectrum of $LiFe_5O_8$ (x = 0) measured at room temperature consists of two Zeeman sextets. These sextets have values of isomer shifts $\delta_1 = 0.27 \pm 0.02$ mm/s and $\delta_2 = 0.35$ mm/s characteristic of Fe^{3+} ions in the tetrahedral and octahedral environments, respectively [42]. The values of the hyperfine magnetic fields of the sextets are H_1 = 497 ± 1 kOe and H_2 = 509 ± 1 kOe. The area of the sextet corresponding to Fe^{3+} ions in the oxygen tetrahedra is A = 40 ± 1 %, and for the sextet related to Fe^{3+} ions in the octahedral environment it is A = 60 ± 1 %, which corresponds to the 2: 3 ratio of the numbers of tetrahedral and octahedral Fe^{3+} sites.

The Mössbauer spectroscopy method is a sensitive tool for probing the local environment of Mössbauer-active cations. According to our results, the isomer shifts of the Mössbauer spectra correspond to Fe^{3+} ions in either tetrahedral or octahedral coordination. Thus, we conclude that our samples do not contain significant quantities of oxygen vacancies.

Mössbauer spectra were also measured at 15 K, i.e., at low temperature, which also helps reducing the effect of relaxation processes on the magnetic structure (Fig. 3). The spectra for the samples with x = 0.7, 0.8, and 0.9 consist of paramagnetic lines described by paramagnetic doublets with the parameters given in Table 2. The isomer shifts of doublets are typical for Fe^{3+} ions in oxygen octahedra. The quadrupole splittings are similar to the values of Δ obtained for the room temperature spectra. It should be noted that the doublet lines of the spectrum of the sample with x = 0.7 are broader than the line of the doublets for the spectra of samples with x = 0.8 and 0.9. This widening probably occurs due to the closeness of the temperature, at which the spectrum was measured (15 K), to the magnetic phase transition temperature. The spectra of samples with x = 0.5 and 0.6 consist of poorly resolved, broadened Zeeman splitting lines. Paramagnetic lines are observed in the spectrum of the sample with x = 0.6. These spectra were interpreted using the $P(H)$ distribution, which are observed to have sets of local maxima. The highest intensity maxima are found at H = 446 ± 1 kOe and 491 ± 1 kOe for the samples with x = 0.5 and 0.6, respectively. The doublet in the spectrum of the sample with x = 0.6 has parameters (Table 2) approximately equal to those of the doublets in the spectra of samples with x = 0.7, 0.8, and 0.9. The structure of the spectra of samples with x = 0.5 and 0.6 is determined by the relaxation of the magnetic moments of Fe^{3+} ions. The spectra of samples with $x \leq 0.4$ consist of two sextets with the parameters given in Table 2. The isomer shifts of the S_1 and S_2 sextets correspond to Fe^{3+} ions in tetrahedral and octahedral oxygen environments, respectively. The areas of the sextets are approximately proportional to the concentrations of Fe^{3+} ions in the corresponding states. The area values of the S_1 sextets decrease with an increase in x from 40 % for x = 0 to 27 ± 1 % for x = 0.4.

Figure 4 shows the Mössbauer spectra of the samples with $0 \leq x \leq 0.4$ measured at a temperature of 720 K. The spectra of the samples with x = 0.3 and 0.4 are paramagnetic doublets with parameters $\delta = 0.07 \pm 0.02$ mm/s and $\Delta = 0.45 \pm 0.02$ mm/s. The spectrum of the sample with x = 0.2 was interpreted using a doublet and the $P(H)$ function. The

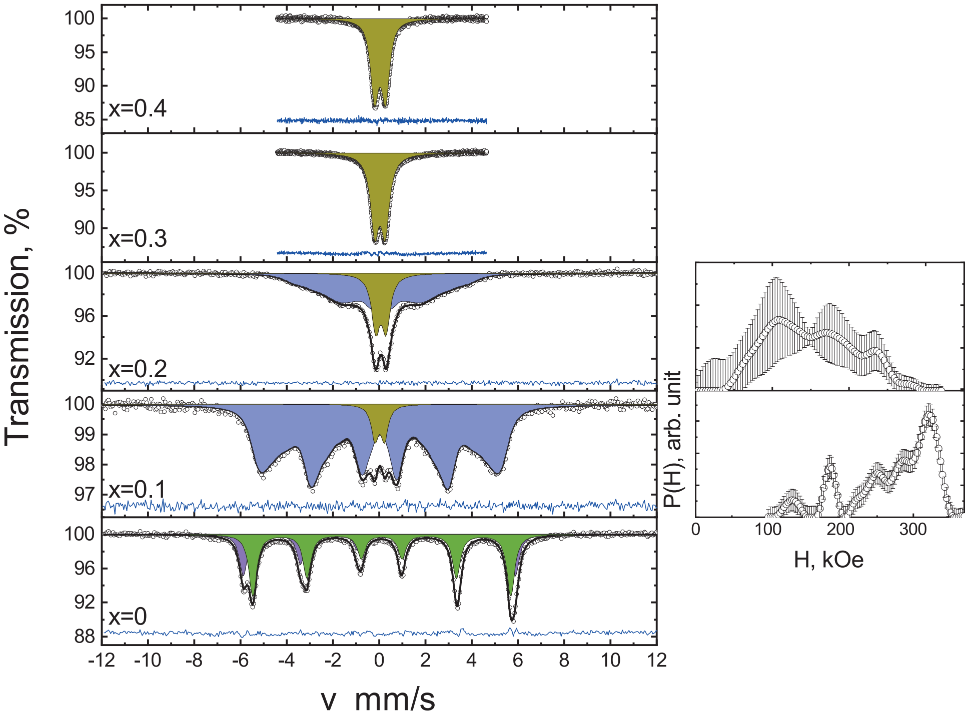

Fig. 4. Mössbauer spectra of the (1-x)$LiFe_5O_8$–(x)$LiZn_{2.5}Ti_{2.5}O_8$ solid solutions taken at 720 K.

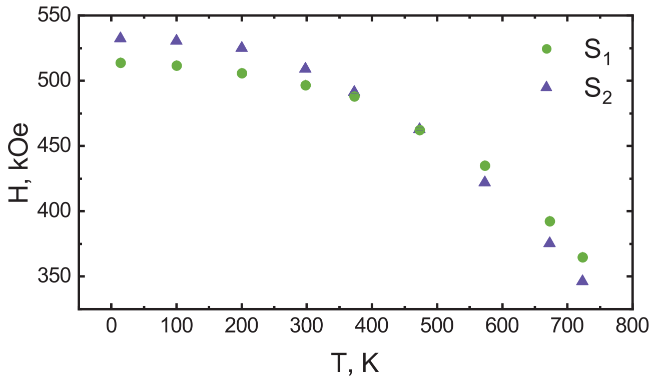

Fig. 5. Temperature dependences of hyperfine magnetic field values for sextets S_1 and S_2 of Mössbauer spectra for the $LiFe_5O_8$ sample.

parameters of the doublet are approximately equal to those observed in the spectra of samples with $x = 0.3$ and 0.4. The function $P(H)$ describes poorly resolved Zeeman splitting lines. The spectrum of the sample with $x = 0.1$ also consists of poorly resolved Zeeman lines, which are described by the function $P(H)$. Poor splitting indicates relaxation of the magnetic moments of iron ions. The spectrum of the sample with $x = 0$ is a superposition of two sextets with parameters $\delta_1 = 0.04 \pm 0.02$ mm/s, $\delta_2 = 0.11 \pm 0.02$ mm/s, $H_1 = 365 \pm 1$ kOe and $H_2 = 346 \pm 1$ kOe. It should be noted that at 15 K in the spectra of samples with $0 \leq x \leq 0.4$, two sextets with different values of δ are observed. At the same time, in the spectra measured at 720 K it is impossible to distinguish the components of the spectra with δ values related to Fe^{3+} with different coordination numbers. This is due to the strong magnetic relaxation, which leads to the indistinguishability of the local environment of Fe^{3+} ions. Such behavior is also observed, for example, in Fe_3O_4 and γ-Fe_2O_3 nanoparticles, in which it is not possible to distinguish the components corresponding to Fe^{3+} ions in the *A*- and *B*-sublattices above the blocking temperature in the Mössbauer spectra [43,44].

In addition, the sextet S_1 of the spectrum of the sample with $x = 0$ measured at 720 K, corresponding to Fe^{3+} ions in the tetrahedral environment, has a higher *H* value than the sextet related to Fe^{3+} ions in the octahedral environment. However, at 15 K, the *H* field is larger in the S_2 sextet (Table 2). In this regard, measurements of the Mössbauer spectra of the $LiFe_5O_8$ sample were made over a wide temperature range. As a result, the temperature dependencies of the fields H_1 and H_2 of the sextets S_1 and S_2, respectively, are obtained in Fig. 5. From the presented data, it can be seen that above 470 K, H_1 becomes greater than H_2.

To determine the temperatures of magnetic phase transitions T_c in (1-x)$LiFe_5O_8$–(x)$LiZn_{2.5}Ti_{2.5}O_8$ the temperature scanning technique was used. This technique is based on the effect of a decrease in the intensity of paramagnetic lines I_m in Mössbauer spectra below the magnetic phase transition temperature, which is due to the transformation of the paramagnetic lines of the spectrum into Zeeman sextets. This approach has been successfully used to determine magnetic ordering temperatures in compounds with the perovskite structure [45–47].

Figure 6(a) shows the dependencies of $I_m(T)$ measured for the LFZT samples. For the $x = 0.2$, 0.3, and 0.4 samples $I_m(T)$ decreases over a wide temperature range. That is, a diffuse magnetic phase transition occurs in these samples over a temperature range of ≈ 200 K. With increasing x, the degree of diffuseness decreases and amounts to ≈ 110 K for the sample with $x = 0.5$ and ≈ 50 K for the sample with $x = 0.6$. Taking the center of the $I_m(T)$ decline on cooling as the magnetic phase transition temperature T_c, the concentration dependence $T_c(x)$ was obtained, which is shown in Fig. 6(b). Therefore, we find that the magnetic phase transition temperature T_c sharply drops above $x \approx 0.5$, which coincides with withdrawal of Fe^{3+} ions from the *A*-sublattice as given in

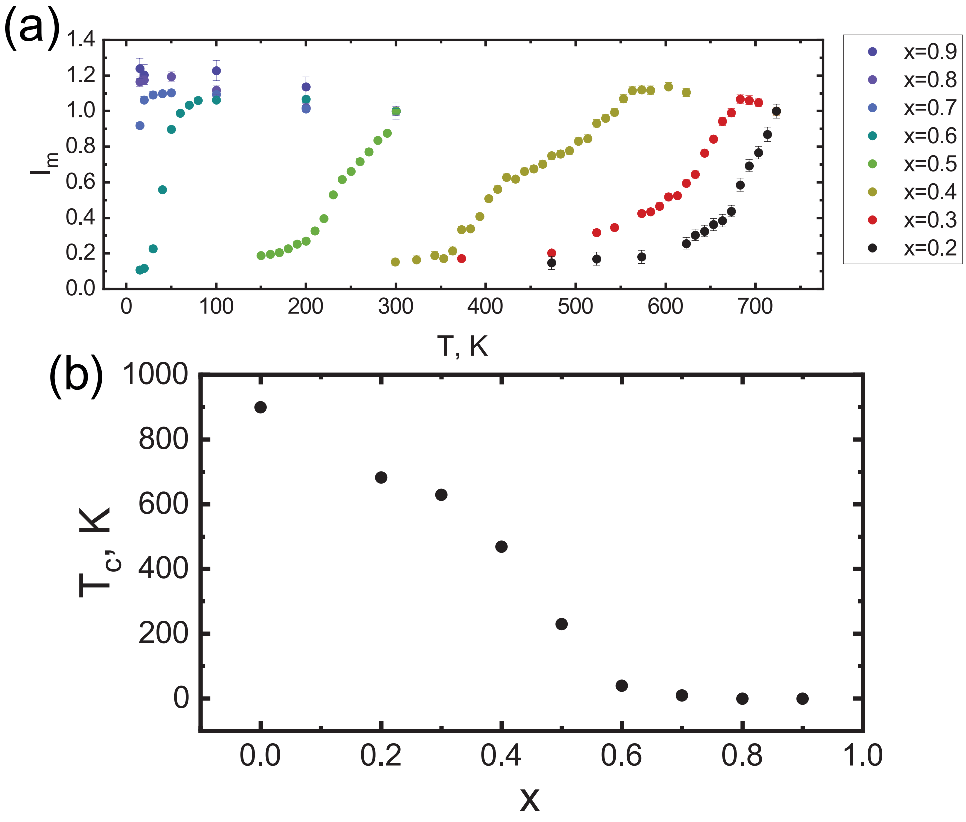

Fig. 6. (a) Temperature dependences of the intensity of paramagnetic lines of the Mössbauer spectra for the samples $(1-x)LiFe_5O_8-(x)LiZn_{2.5}Ti_{2.5}O_8$. (b) Dependence of magnetic phase transition temperature $T_c(x)$ on concentration x in $(1-x)LiFe_5O_8-(x)LiZn_{2.5}Ti_{2.5}O_8$.

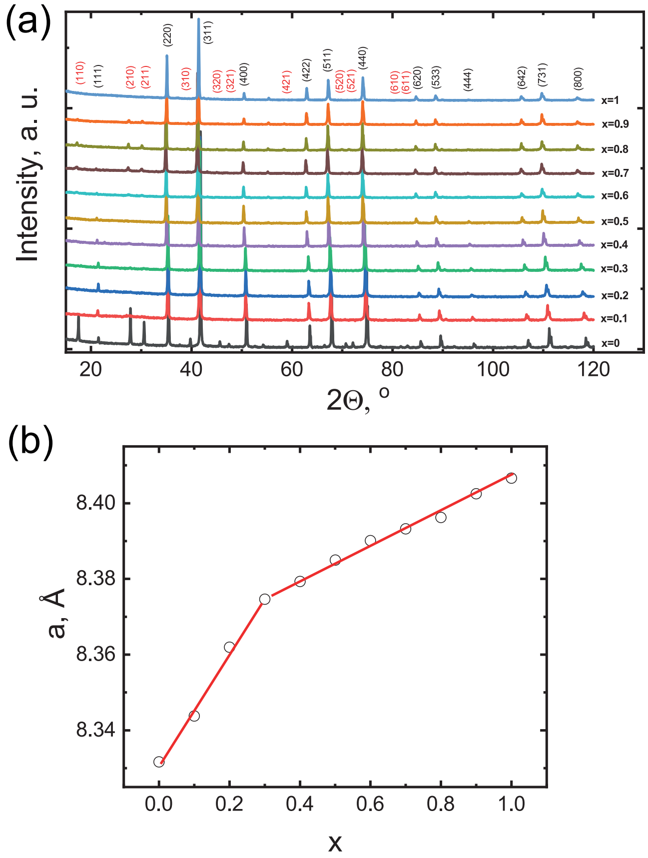

Fig. 7. (a) X-ray diffraction profiles of the (1-x)LiFe$_5$O$_8$–(x)LiZn$_{2.5}$Ti$_{2.5}$O$_8$ solid solutions. (b) Dependence of the cubic lattice parameter a on concentration x.

Table 3
Proposed substitution schemes in cationic sublattices in the (1-x)LiFe$_5$O$_8$–(x) LiZn$_{2.5}$Ti$_{2.5}$O$_8$ system.

x	A-sublattice	B-sublattice	Phase
0.1	$Zn^{2+} \longrightarrow$ (8a) Fe^{3+}	$Ti^{4+} \longrightarrow$ (16c) Fe^{3+}	$\beta - LiFe_5O_8$
$0.2 \leq x \leq 0.5$	$Zn^{2+} \longrightarrow$ (8a) Fe^{3+} $Li^{+} \longrightarrow$ (8a) Fe^{3+}	$Ti^{4+} \longrightarrow$ (16c) Fe^{3+} $Fe^{3+} \longrightarrow$ (16c) Li^{+}	$\beta - LiFe_5O_8$
$0.6 \leq x \leq 0.7$	$Zn^{2+} \longrightarrow$ (8c) Fe^{3+} $Li^{+} \longrightarrow$ (8c) Fe^{3+}	$Ti^{4+} \longrightarrow$ (12d) Fe^{3+} $Fe^{3+} \longrightarrow$ (4b) Li^{+}	$\alpha - LiFe_5O_8$
0.8	$Zn^{2+} \longrightarrow$ (8c) Fe^{3+}	$Ti^{4+} \longrightarrow$ (12d) Fe^{3+}	$\alpha - LiFe_5O_8$
0.9	$Zn^{2+} \longrightarrow$ (8c) Fe^{3+}	$Ti^{4+} \longrightarrow$ (12d) Fe^{3+} $Zn^{2+} \longrightarrow$ (12d) Fe^{3+}	$\alpha - LiFe_5O_8$
1.0	$Zn^{2+} \longrightarrow$ (8a) Fe^{3+}	$Ti^{4+} \longrightarrow$ (16c) Fe^{3+} $Zn^{2+} \longrightarrow$ (16c) Fe^{3+}	$\beta - LiFe_5O_8$

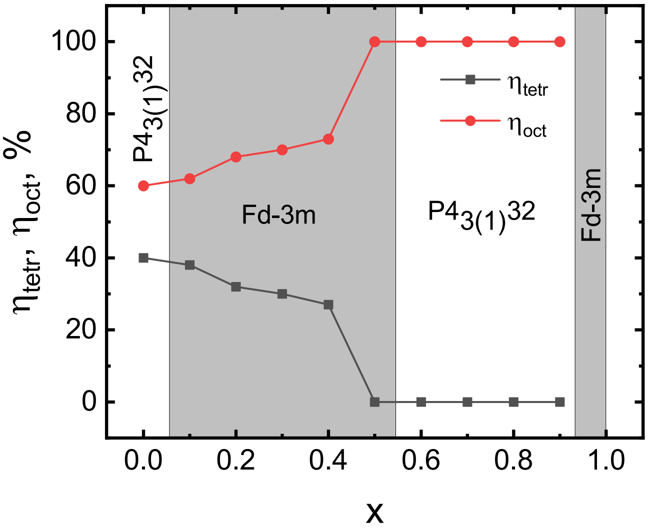

Fig. 8. Percentage of iron in tetrahedral (η_{tetr}) and octahedral (η_{oct}) environments as functions of x.

Table 2.

3.2. X-ray diffraction

Figure 7(a) shows X-ray diffraction profiles of the (1-x)LiFe$_5$O$_8$–(x) LiZn$_{2.5}$Ti$_{2.5}$O$_8$ ($0 \leq x \leq 1$) solid solutions. The X-ray data reveal that a complete series of solid solutions over the entire concentration range are formed. Diffraction peaks belonging to a typical cubic spinel-type structure are present at any value of x. For several concentrations, structural reflexes have been identified, such as (110), (210), (211), (310), (320), (321), (421), (520), (521), (610), and (611) indicated by the red font in Fig. 7(a), which reflect ordering of cations in the octahedral B-sublattice according to the 1:3 type. This atomic ordering can be complete or partial and is observed for $x = 0$, 0.6, 0.7, 0.8, and 0.9. Moreover, at $x = 0$, all superstructural peaks, including low-intensity ones, are identified, which indicates the complete ordering of Li^+ and Fe^{3+} cations in the B-sublattice in the ratio 1:3. For $x = 0.6$, 0.7, 0.8, and 0.9, only the most intense superstructural peaks are observed, such as (210) and (211), which indicates partial ordering only. In these cases, the α-LiFe$_5$O$_8$ phase is formed (sp. gr. P4$_{3(1)}$32) [48]. For $x = 0.1$, 0.2, 0.3, 0.4, 0.5, and 1 no superstructural peaks are observed. Thus, these samples crystallize according to the β-LiFe$_5$O$_8$ type (sp. gr. Fd$\overline{3}$m) [17].

Based on the data presented in Fig. 7(a), it can be seen that in the case of $0.1 \leq x \leq 0.5$, already a small ion substitution of Fe^{3+} by the Zn^{2+} and Ti^{4+} ions leads to complete destruction of the ordered phase, which is confirmed by the disappearance of all superstructural peaks. The structure of the obtained solid solutions corresponds to the disordered phase of β-LiFe$_5$O$_8$ [17]. Then, in the cases $0.6 \leq x \leq 0.9$, when more than half of the Fe^{3+} ions are replaced, local ordering of cations occurs again in the octahedral B-sites. However, the degree of atomic ordering is small, since only the most intense superstructural peaks (210) and (211) are observed in the X-ray profiles. Finally, at $x = 1$, when all Fe^{3+} ions are completely replaced, the ordered arrangement of cations in the B-sublattice again disappears and a completely disordered β-LiFe$_5$O$_8$-type phase is formed.

It is well-known that different cations in spinels have different preferences for occupation of tetrahedral and octahedral sites. In the case of LFZT the preference of cations for occupation of the B-sites in order of increasing preference is Zn^{2+}, Fe^{3+}, Li^+, Ti^{4+} [27]. In accordance with this series, a logical assumption can be made that in the A-sublattice Fe^{3+} is replaced by Zn^{2+}, and in the B-sublattice Fe^{3+} is replaced by Ti^{4+}. However, the obtained experimental data suggest that the substitution scheme does not fully correspond to the above. Based on the Mössbauer spectroscopy data and the X-ray diffraction analysis the proposed substitution schemes are presented in Table 3.

In the sample with $x = 0.1$, as expected, in the tetrahedral A-sublattice Fe^{3+} ions are replaced by Zn^{2+}, and in the octahedral B-sublattice, Fe^{3+} ions are replaced by Ti^{4+}. In the case $0.2 \leq x \leq 0.5$, in addition to the expected substitutions, partial exchange of Fe^{3+} ions in the A-sites with the Li^+ ions in the B-site takes place. This results in a disordered β-LiFe$_5$O$_8$ phase. In the concentration range $0.6 \leq x \leq 0.7$, similar ion substitutions and redistributions are observed, however, partial atomic ordering in octahedral positions takes place in these compounds, i.e., the α-LiFe$_5$O$_8$ phase is formed. Hence, this phenomenon of redistribution of Fe^{3+} and Li^+ ions in sublattices does not depend on the presence of atomic order in the structure. In the case of $x = 0.8$, Zn^{2+} ions completely replace Fe^{3+} ions in the A-sublattice, and in the B-sublattice, the regular substitution by Ti^{4+} continues. At $x = 0.9$, we can observe the simultaneous substitution of Fe^{3+} ions by Zn^{2+} in the A- and

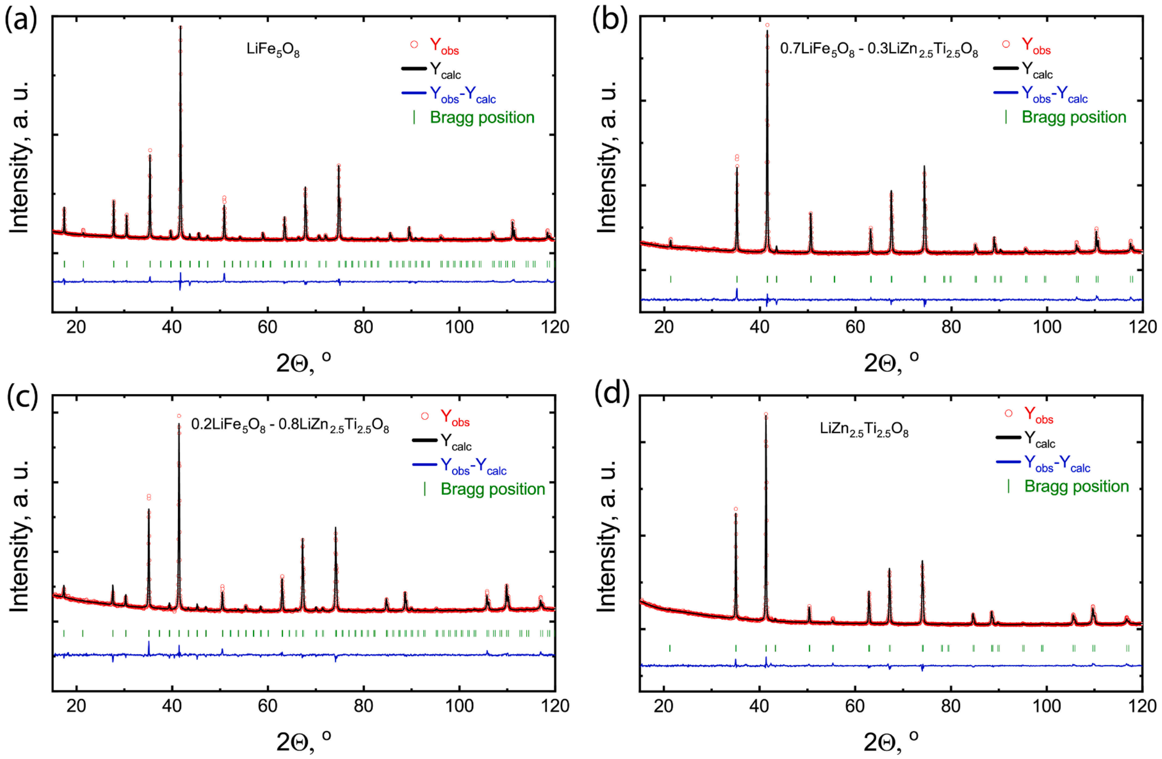

Fig. 9. Rietveld refinement of LFZT solid solutions with (a) $x = 0$, (b) $x = 0.3$, (c) $x = 0.8$, and (d) $x = 1$.

B-sublattices, since the amount of introduced Zn^{2+} exceeds the number of tetrahedral positions. In both cases, the phenomenon of the transition of part of the Li^{+} ions from the octahedral sublattice to the tetrahedral one is not observed. When Fe^{3+} ions are completely replaced, partial ordering in the *B*-sublattice is destroyed, tetrahedral positions are occupied only by zinc ions, and octahedral positions are occupied by lithium, titanium, and zinc ions.

Assumptions about the substitution schemes were made based on the study of the local crystalline environment of iron ions by the Mössbauer spectroscopy Table 3. The dependencies of the percentage of iron in tetrahedral (η_{tetr}) and octahedral (η_{oct}) environments on concentration are shown in Fig. 8.

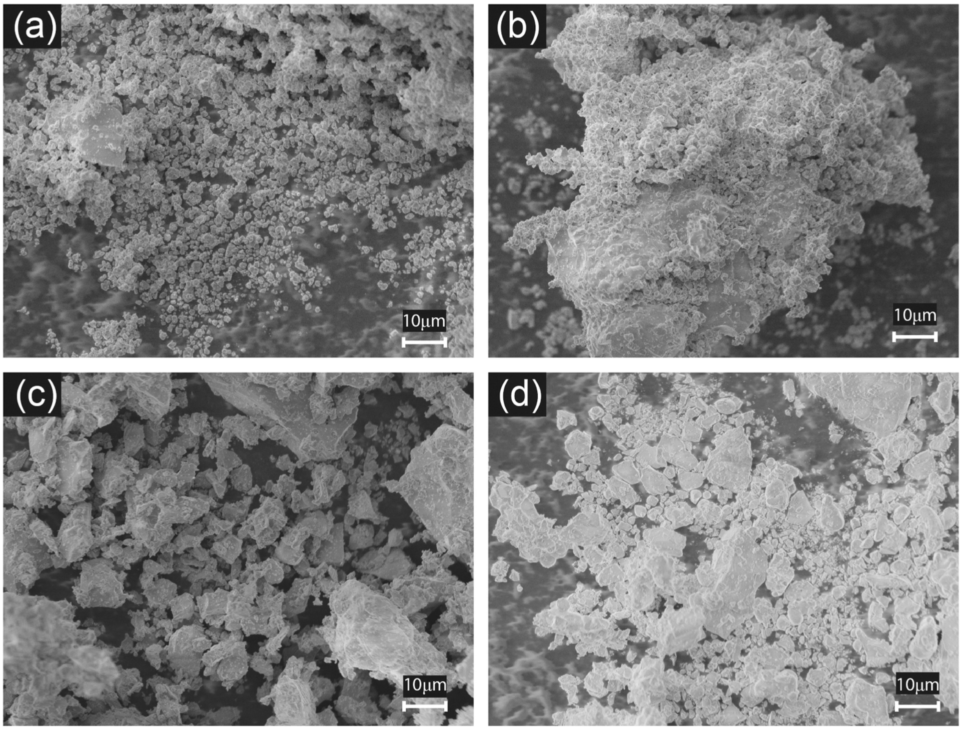

Fig. 10. SEM microphotographs of samples (a) $x = 0.1$, (b) $x = 0.3$, (c) $x = 0.5$, and (d) $x = 0.9$.

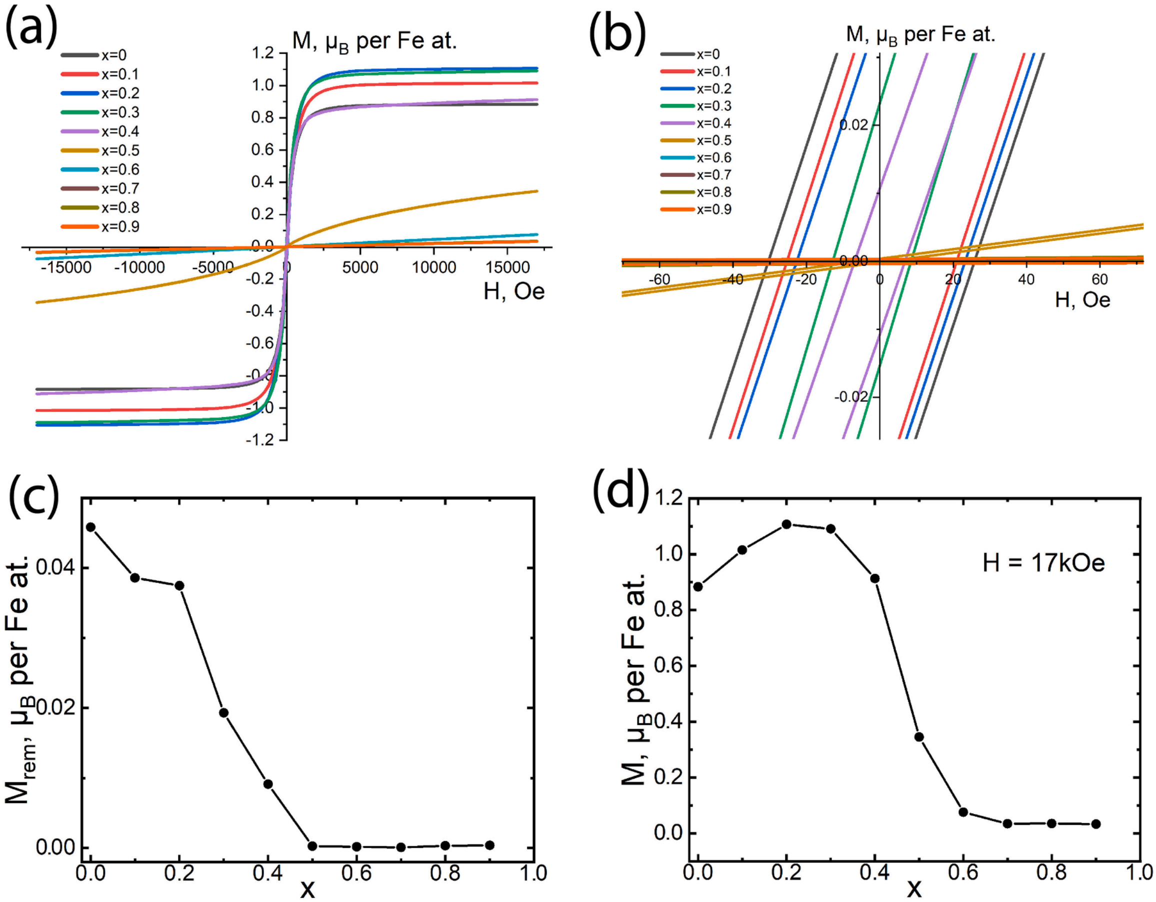

Fig. 11. (a) Magnetization as function of applied magnetic field. (b) Central part of the $M(H)$ hysteresis loops of (a). (c) Remnant magnetization for different x. (d) Magnetization at $H = 17$ kOe for different x.

The cell parameters of (1-x)LiFe$_5$O$_8$–(x)LiZn$_{2.5}$Ti$_{2.5}$O$_8$ were refined by full-profile analysis using the Rietveld algorithm. Based on the values of the ion radii obtained by Shannon [49] for the six-coordinated Zn^{2+} (0.74 Å), Fe^{3+} (0.645 Å), Li^{+} (0.76 Å), Ti^{4+} (0.605 Å) and four-coordinated Zn^{2+} (0.60 Å), Fe^{3+} (0.49 Å), Li^{+} (0.59 Å), it can be concluded that the simultaneous substitution of zinc and titanium for iron should lead to an increase of the cell parameter. The experimental dependence of the refined cell parameters for the studied compounds increases with x as shown in Fig. 7(b). Two qualitatively different regions can be distinguished, i.e., the first region with $0 \leq x \leq 0.3$ and the second one with $0.3 \leq x \leq 1$, which can be fitted with linear functions with different slopes. This can be explained by a change in the substitution mechanism of ions, as well as by the phenomenon of the transition of some Li^{+} ions from an octahedral sublattice to a tetrahedral one.

The structures of the obtained solid solutions were refined using the Rietveld method. Fig. 9 shows the results for four selected samples. As the initial model for the ordered samples ($x = 0$ and $0.6 \leq x \leq 0.9$), the structural model of α-LiFe$_5$O$_8$ (sp. gr. P4$_{3(1)}$32) was used [34], whereas for the disordered samples ($0.1 \leq x \leq 0.5$ and $x = 1$) the β-LiFe$_5$O$_8$ structure (sp. gr. Fd$\bar{3}$m) was used [35]. The data presented in Fig. 8 and Table 2 were used to fix the position of iron ions in the structure. The refined models confirm the substitution mechanism proposed in Table 3, and are also consistent with the results of the Mössbauer spectroscopy studies. The molecular formula of the two solid solutions shown in Fig. 9 can be written as [(Li$_{0.2}$Zn$_{0.75}$Fe$_{1.05}$)(Li$_{0.8}$Fe$_{2.45}$Ti$_{0.75}$)O$_8$] for $x = 0.3$ and [(Zn$_2$)(LiFeTi$_2$)O$_8$] for $x = 0.8$.

3.3. Scanning electron microscopy

Microstructural analysis of a series of solid solutions (1-x)LiFe$_5$O$_8$–(x)LiZn$_{2.5}$Ti$_{2.5}$O$_8$ showed that the average particle size increases with increasing x value. Based on the data presented in the Fig. 10(a), in the case of $0 \leq x \leq 0.2$, most of the powder consists of small-sized crystallites (about 0.5 – 3μm), which stick together to form irregularly shaped conglomerates with dimensions around 5 – 10μm. Fig. 10(b) shows the microphotography of the sample $x = 0.3$, there is a large irregularly-shaped crystallite measuring approximately 80 × 60 × 15μm, which is plastered over by other smaller ones with dimensions on the order of 1 – 3μm. Based on the data presented in Fig. 10(c), we observe the formation of larger crystallites with a regular shape and sharp corners in samples $0.4 \leq x \leq 0.8$. Fig. 10(d) shows the SEM data of the sample with $x = 0.9$, we find small crystallites of size 1 – 3μm predominating over larger ones. It is also possible to detect the presence of middle-sized crystals around 5 – 7μm, while large crystals of 8 – 10μm are much fewer.

3.4. Magnetic measurements and MC calculations

Figure 11(a) shows magnetic hysteresis loops $M(H)$ for the LFZT solid solutions measured at room temperature and Fig. 11(b) gives enlarged central part of the $M(H)$ curves. The samples with $0 \leq x \leq 0.4$ reveal a ferrimagnetic behaviour with small remnant magnetization as shown in Fig. 11(c). For $x \geq 0.5$ the remnant magnetization vanishes and the solid solutions become paramagnetic at room temperature.

Figure 11(d) gives magnetization at $H = 17$ kOe. It can be seen that for small x the magnetization initially grows with substitution

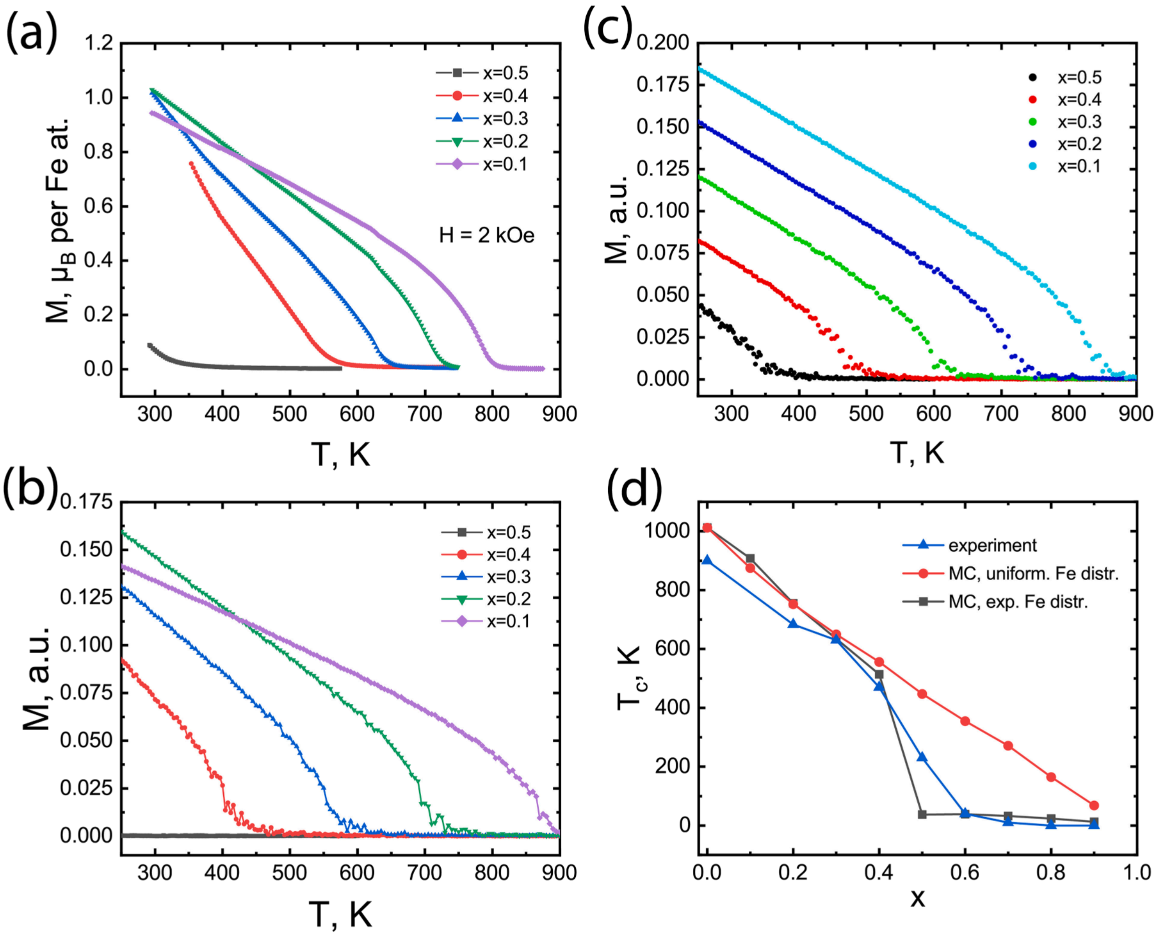

Fig. 12. (a) Dependence of magnetization on temperature for selected LFZT solid solutions. (b) and (c) calculated $M(T)$ dependencies with the experimental and uniform distributions of Fe^{3+} ions, respectively. (d) Experimentally determined and calculated $T_c(x)$ dependencies.

experiencing a maximum at $x \approx 0.2$ and drops rapidly with further increase of x. From our point of view such magnetic behaviour is due to the following. At $x = 0.1$ each Zn and Ti atom substitutes Fe in the *A*- and *B*-sublattices, respectively. This results in a relatively higher ratio of substitution of non-magnetic ions for Fe in the tetrahedral sublattice compared to that in the octahedral one because the number of tetrahedral sites is smaller than that in the octahedral sublattice. Therefore, it leads to different changes in the magnetizations of both sublattices resulting in relative increase of *B*-sublattice magnetization compared to that of the *A*-sublattice with antiparallel magnetization. At $x = 0.2$ in addition to the Zn and Ti substitution for Fe in both sublattices, there occurs further exchange of Fe from the tetrahedral positions with the Li atoms from octahedral ones as discussed in Sec. 3.2, which results in the further growth of the difference between magnetizations of the *B*- and *A*-sublattices and an increase in total magnetization. However, in the sample with $x = 0.3$ overall dilution of magnetic ions finally results in decrease in total magnetization despite the relatively higher number of Fe ions in the octahedral sites.

Figure 12(a) shows the temperature dependence of magnetization in the samples with $0.1 \leq x \leq 0.5$. With decreasing temperature, the magnetization $M(T)$ rapidly grows below T_c and the T_c values gradually decrease with growing x for $0.1 \leq x \leq 0.4$. In contrast, the T_c value for $x = 0.5$ drastically drops compared to that of the $x = 0.4$ sample and the $M(T)$ starts growing only below room temperature.

Figure 12(b) shows $M(T)$ curves as calculated using the MC method. In this calculation we assumed the distribution of Fe^{3+} ions between the *A*- and *B*-sublattices according to the results of Mössbauer measurements shown in Fig. 8. One can note good qualitative correspondence of the calculated $M(T)$ dependencies with the experimental results including the crossover of the curves for $x = 0.1$ and $x = 0.2$, as wells as the drastic drop of T_c for the $x = 0.5$ sample. For comparison, in Fig. 12(c) we present the results of MC calculations for the case of uniform substitution of Fe^{3+} ions in both the *A*- and *B*-sublattices with increasing x. Such substitution results in gradual suppression of the magnetic properties of LFZT solid solutions with increasing x.

Figure 12(d) combines the experimentally determined $T_c(x)$ dependencies with those calculated using the MC method. One can note good correspondence between the experimental data and the MC calculations based on the experimental Fe^{3+} distribution. Both $T_c(x)$ curves experience big drop at $x \approx 0.5$, which is to be contrasted with the steady decrease of $T_c(x)$ with growing x for the case of uniform Fe^{3+} distribution.

4. Discussion

The system (1-x)$LiFe_5O_8$–(x)$LiZn_{2.5}Ti_{2.5}O_8$ forms a complete series of solid solutions. The Mössbauer measurements reveal that the substitution of Zn^{2+} and Ti^{4+} ions for Fe^{3+} occurs rather uniform in both cationic sublattices *A* and *B* up to $x \approx 0.4$ as shown in Fig. 8. Above $x = 0.5$ the number of Fe^{3+} ions at the tetrahedral sites vanishes and all iron resides in the *B*-sublattice.

Both the Mössbauer spectroscopy and magnetic measurements reveal that the magnetic phase transition temperature T_c gradually decreases with increasing x up to $x \approx 0.4$ and experiences a sharp drop at $x = 0.5$ with near-zero values for $x \geq 0.6$ as depicted in Fig. 6(b). Thus, this suppression of magnetic properties coincides with the drop in occupation of the A-sublattice by Fe^{3+} ions.

The studied solid solutions reveal a rather uncommon progression of ordered and disordered phases with increasing concentration x. The concentrational phase diagram (Fig. 8) shows two disordered spinel phases with the Fd$\overline{3}$m symmetry and two regions with 1:3 at. ordering in the B-sublattice with the P4$_{3(1)}$32 space group. A similar concentration-induced cationic ordering has been observed in $Li_{4/3-2x/3}Zn_xTi_{5/3-x/3}O_4$ at $x = 0.25$ and $(1-x)LiFe_5O_8 - xLi_2ZnTi_3O_8$ at $x = 0.1$ and 0.75 [27,50]. From our point of view this succession of ordered and disordered phases has little impact on the magnetic properties as can be inferred from the comparison of the difference of magnetic behaviour of the $x = 0$ and $x = 0.1$ cases, which is mostly due to 10 % difference in the number of magnetic Fe^{3+} ions between the samples.

The observed magnetic behaviour is confirmed by MC calculations. From DFT calculations it follows that the strongest magnetic exchange constants are within the nearest neighbour $A - B$ pairs (J_{AB}) as given in Table 1. All exchange constants are antiferromagnetic in nature and the strong J_{AB} interactions result in ferrimagnetic behaviour since the numbers of Fe^{3+} cations in the sublattices A and B are different [51]. With increasing x the number of Fe^{3+} cations in the A-sublattice sharply drops at $x \approx 0.5$, which results in elimination of the strongest magnetic exchange interactions and a consequent sharp drop in T_c and suppression of magnetic properties. Upon approaching this critical x value the dilution of the A-sublattice results in large broadening of magnetic phase transitions in samples with $0.2 \leq x \leq 0.4$.

5. Conclusions

We have synthesized (1-x)$LiFe_5O_8$–(x)$LiZn_{2.5}Ti_{2.5}O_8$ spinel solid solutions in the whole concentration range x. The solid solutions experience complex concentrational phase diagram with alternating ordered and disordered phases. Nonlinear dependence of Fe^{3+} ion occupation on concentration x results in strong suppression of magnetic properties for $x \geq 0.5$ when all iron resides in the B-sublattice. The magnetic exchange constants for $LiFe_5O_8$ are determined for the first time by the density functional theory. Monte Carlo calculations confirm the observed magnetic behaviour, which is dominated by strong antiferromagnetic interlattice $A - B$ exchange between nearest neighbours.

CRediT authorship contribution statement

N.V. Ter-Oganessian: Writing – review & editing, Writing – original draft, Supervision, Project administration, Investigation, Conceptualization. **A.V. Nazarenko:** Investigation. **Yu.V. Rusalev:** Investigation. **S.A. Guda:** Investigation. **A.S. Komlev:** Investigation. **S.P. Kubrin:** Writing – original draft, Investigation. **A.V. Motseyko:** Writing – original draft, Investigation. **A.A. Zabolotnyi:** Writing – review & editing, Writing – original draft, Investigation.

Declaration of Competing Interest

The authors declare that they have no known competing financial interests or personal relationships that could have appeared to influence the work reported in this paper.

Data Availability

No data was used for the research described in the article.

Acknowledgements

This work was financially supported by the Ministry of Science and Higher Education of the Russian Federation (State assignment in the field of scientific activity, Southern Federal University, 2023, Project No. FENW-2023–0015).

References

[1] Q. Zhao, Z. Yan, C. Chen, J. Chen, Spinels: Controlled preparation, oxygen reduction/evolution reaction application, and beyond, Chem. Rev. 117 (15) (2017) 10121–10211, https://doi.org/10.1021/acs.chemrev.7b00051.

[2] S. Yuvaraj, M.-S. Park, V.G. Kumar, Y.S. Lee, D.-W. Kim, Electrochemical performance of M_2 GeO_4 (M= Co, Fe and Ni) as anode materials with high capacity for lithium-ion batteries, J. Electrochem. Sci. Techn. 8 (4) (2017) 323–330, https://doi.org/10.5229/JECST.2017.8.4.323.

[3] Y.J. Lee, S.-H. Park, C. Eng, J.B. Parise, C.P. Grey, Cation ordering and electrochemical properties of the cathode materials $LiZn_x$ Mn_{2-x} O_4, $0 < x \leq 0.5$: A ^{6} Li magic-angle spinning NMR spectroscopy and diffraction study, Chem. Mater. 14 (1) (2002) 194–205, https://doi.org/10.1021/cm010503.

[4] E. Lysenko, V. Vlasov, A. Malyshev, E. Sheveleva, A. Surzhikov, Microstructure and electromagnetic properties of $LiFe_5$ O_8 ferrite ceramics prepared from wet-and dry-milled powders, Ceram. Int. 47 (17) (2021) 23935–23941, https://doi.org/10.1016/j.ceramint.2021.05.102.

[5] N. Rezlescu, C. Doroftei, E. Rezlescu, P. Popa, Lithium ferrite for gas sensing applications, Sens. Actuators B 133 (2) (2008) 420–425, https://doi.org/10.1016/j.snb.2008.02.047.

[6] F. Xie, H. Liu, M. Bai, S. Wen, F. Xu, J. Zhao, W. Liu, Flexible LiZnTiMn ferrite/PDMS composites with enhanced magnetic-dielectric properties for miniaturized application, Ceram. Int. 47 (1) (2021) 1121–1125, https://doi.org/10.1016/j.ceramint.2020.08.228.

[7] A. Sundaresan, N.V. Ter-Oganessian, Magnetoelectric and multiferroic properties of spinels, J. Appl. Phys. 129 (6) (2021) 060901, https://doi.org/10.1063/5.0035825.

[8] Y. Okamoto, G.J. Nilsen, J.P. Attfield, Z. Hiroi, Breathing pyrochlore lattice realized in A-site ordered spinel oxides $LiGaCr_4$ O_8 and $LiInCr_4$ O_8, Phys. Rev. Lett. 110 (2013) 097203, https://doi.org/10.1103/PhysRevLett.110.097203.

[9] Y.A. Kesler, E.G. Zhukov, D.S. Filimonov, E.S. Polulyak, T.K. Menshchikova, V. A. Fedorov, $CuCr_2$ S_4 -based quaternary cation-substituted magnetic phases, Inorg. Mater. 41 (2005) 914, https://doi.org/10.1007/s10789-005-0236-4.

[10] H.M. Palmer, C. Greaves, Structural, magnetic and electronic properties of $Fe_{0.5}$ $Cu_{0.5}$ Cr_2 S_4, J. Mater. Chem. 9 (1999) 637, https://doi.org/10.1039/A809032G.

[11] T.G. Aminov, D.I. Kirdyankin, G.G. Shabunina, V.M. Novotortsev, Magnetic properties of $Cu_{0.5}$ $Fe_{0.5-x}$ Ga_x Cr_2 S_4 solid solutions, Russ. J. Inorg. Chem. 57 (2012) 991, https://doi.org/10.1134/S0036023612070030.

[12] N.V. Ter-Oganessian, Cation-ordered $A'_{1/2}$ $A''_{1/2}$ B_2 X_4 magnetic spinels as magnetoelectrics, J. Magn. Magn. Mater. 364 (2014) 47–54, https://doi.org/10.1016/j.jmmm.2014.04.019.

[13] Y. Lin, J. Dong, J. Dai, J. Wang, H. Yang, H. Zong, Facile synthesis of flowerlike $LiFe_5$ O_8 microspheres for electrochemical supercapacitors, Inorg. Chem. 56 (24) (2017) 14960–14967, https://doi.org/10.1021/acs.inorgchem.7b02257.

[14] P. Braun, A superstructure in spinels, Nature 170 (4339) (1952) 1123, https://doi.org/10.1038/1701123a0.

[15] M. Iliev, V. Ivanov, N. Todorov, V. Marinova, M. Abrashev, R. Petrova, Y.-Q. Wang, A. Litvinchuk, Lattice dynamics of the α and β phases of $LiFe_5$ O_8, Phys. Rev. B 83 (17) (2011) 174111, https://doi.org/10.1103/PhysRevB.83.174111.

[16] A. Smolentsev, A. Meshalkin, N. Podberezskaya, A. Kaplun, Refinement of $LiFe_5$ O_8 crystal structure, J. Struct. Chem. 49 (2008) 953–956, https://doi.org/10.1007/s10947-008-0163-8.

[17] J. Darul, W. Nowicki, P. Piszora, C. Baehtz, E. Wolska, Synchrotron X-ray powder diffraction studies on the order–disorder phase transition in lithium ferrites, J. All. Comp. 401 (1-2) (2005) 60–63, https://doi.org/10.1016/j.jallcom.2005.02.058.

[18] G. Velleaud, M. Mercier, J. Puvinel, G. Aubert, P. Escudier, Magnetoelectric effect and magnetization process in Fe_5 LiO_8, Solid State Commun. 27 (7) (1978) 729–733, https://doi.org/10.1016/0038-1098(78)90013-3.

[19] R. Liu, L. Pan, S. Peng, L. Qin, J. Bi, J. Wu, H. Wu, Z.-G. Ye, The magnetoelectric effect in a cubic ferrimagnetic spinel $LiFe_5$ O_8 with high coupling temperature, J. Mater. Chem. C. 7 (7) (2019) 1999–2004, https://doi.org/10.1039/C8TC05615C.

[20] P.V.B. Reddy, B. Ramesh, C.G. Reddy, Electrical conductivity and dielectric properties of zinc substituted lithium ferrites prepared by sol–gel method, Phys. B 405 (7) (2010) 1852–1856, https://doi.org/10.1016/j.physb.2010.01.062.

[21] H. Demidzu, T. Nakamura, Y. Yamada, Synthesis and magnetic properties of Li–Mn–Zn spinel oxides, J. Magn. Magn. Mater. 322 (13) (2010) 1816–1821, https://doi.org/10.1016/j.jmmm.2009.12.033.

[22] G. White, C. Patton, Magnetic properties of lithium ferrite microwave materials, J. Magn. Magn. Mater. 9 (4) (1978) 299–317, https://doi.org/10.1016/0304-8853(78)90085-9.

[23] C.E. Patton, C.A. Edmondson, Y.H. Liu, Magnetic properties of lithium zinc ferrite, J. Appl. Phys. 53 (3) (1982) 2431–2433, https://doi.org/10.1063/1.330835.

[24] R. Sangshetti, V. Hiremath, V. Jali, Combustion synthesis and structural characterization of Li–Ti mixed nanoferrites, Bull. Mater. Sci. 34 (2011) 1027–1031, https://doi.org/10.1007/s12034-011-0160-y.

[25] A. Gruskova, J. Slama, R. Dosoudil, M. Ušáková, V. Jančárik, E. Ušák, Microwave properties of some substituted LiZn ferrites, J. Magn. Magn. Mater. 320 (20) (2008) e860–e864, https://doi.org/10.1016/j.jmmm.2008.04.131.

[26] A. Grusková, V. Jančárik, J. Sláma, R. Dosoudil, Effect of Zn–Ti substitution on electromagnetic properties of Li ferrites, J. Magn. Magn. Mater. 304 (2) (2006) e762–e765, https://doi.org/10.1016/j.jmmm.2006.02.214.

[27] L. He, S.-B. Mi, X. Jin, H. Zhang, D. Zhou, F. Xiang, H. Yang, H. Wang, Order–Disorder phase transition and magneto-dielectric properties of (1-x)LiFe$_5$ O$_8$ –xLi$_2$ ZnTi$_3$ O$_8$ spinel-structured solid solution ceramics, J. Am. Ceram. Soc. 98 (7) (2015) 2122–2129, https://doi.org/10.1111/jace.13547.

[28] M. Kavanlooee, B. Hashemi, H. Maleki-Ghaleh, J. Kavanlooee, Effects of annealing on phase evolution, microstructure, and magnetic properties of nanocrystalline ball-milled LiZnTi ferrite, J. Electr. Mater. 41 (2012) 3082–3086, https://doi.org/10.1007/s11664-012-2235-y.

[29] R. Saha, R. Dhanya, C. Bellin, K. Béneut, A. Bhattacharyya, A. Shukla, C. Narayana, E. Suard, J. Rodríguez-Carvajal, A. Sundaresan, Magnetostructural coupling and magnetodielectric effects in the α -site cation-ordered spinel LiFeCr$_4$ O$_8$, Phys. Rev. B 96 (2017) 214439, https://doi.org/10.1103/PhysRevB.96.214439.

[30] Y. Okamoto, T. Kanematsu, Y. Kubota, T. Yajima, K. Takenaka, Large magnetic-field-induced strain at the spin-reorientation transition in A-site ordered spinel oxide LiFeCr$_4$ O$_8$, J. Phys. Soc. Jpn. 91 (2) (2022) 023710, https://doi.org/10.7566/JPSJ.91.023710.

[31] R. Saha, F. Fauth, M. Avdeev, P. Kayser, B.J. Kennedy, A. Sundaresan, Magnetodielectric effects in *A* -site cation-ordered chromate spinels Li*M* Cr$_4$ O$_8$ (*M* = Ga and In, Phys. Rev. B 94 (2016) 064420, https://doi.org/10.1103/PhysRevB.94.064420.

[32] J. Rodríguez-Carvajal, Full-.-., CEA/Saclay, Fr. 1045 (2001) 132–146.

[33] T. Roisnel, J. Rodriguez-Carvajal, WinPLOTR: A Windows tool for powder diffraction pattern analysis, 78, 2001, 118-123.10.4028/www.scientific.net/MSF.378-381.118.

[34] S. Marin, M. O'Keeffe, D. Partin, Structures and crystal chemistry of ordered spinels: LiFe$_5$ O$_8$, LiZnNbO$_4$, and Zn$_2$ TiO$_4$, J. Solid State Chem. 113 (2) (1994) 413–419, https://doi.org/10.1006/jssc.1994.1389.

[35] F. de Boer, J.H. van Santen, E.J.W. Verwey, The electrostatic contribution to the lattice energy of some ordered spinels, J. Chem. Phys. 18 (8) (2004) 1032–1034, https://doi.org/10.1063/1.1747852.

[36] M.E. Matsnev, V.S. Rusakov, SpectrRelax: an application for Mössbauer spectra modeling and fitting, AIP Conf. Proc. 1489 (1) (2012) 178–185, https://doi.org/10.1063/1.4759488.

[37] G. Kresse, J. Furthmüller, Efficient iterative schemes for *ab initio* total-energy calculations using a plane-wave basis set, Phys. Rev. B 54 (1996) 11169, https://doi.org/10.1103/PhysRevB.54.11169.

[38] P.E. Blöchl, Projector augmented-wave method, Phys. Rev. B 50 (1994) 17953, https://doi.org/10.1103/PhysRevB.50.17953.

[39] J.P. Perdew, K. Burke, M. Ernzerhof, Generalized gradient approximation made simple, Phys. Rev. Lett. 77 (1996) 3865–3868, https://doi.org/10.1103/PhysRevLett.77.3865.

[40] S.L. Dudarev, G.A. Botton, S.Y. Savrasov, C.J. Humphreys, A.P. Sutton, Electron-energy-loss spectra and the structural stability of nickel oxide: an LSDA+U study, Phys. Rev. B 57 (1998) 1505, https://doi.org/10.1103/PhysRevB.57.1505.

[41] K. Momma, F. Izumi, VESTA 3 for three-dimensional visualization of crystal, volumetric and morphology data, J. Appl. Cryst. 44 (2011) 1272–1276, https://doi.org/10.1107/S0021889811038970.

[42] F. Menil, Systematic trends of the 57Fe Mössbauer isomer shifts in (FeOn) and (FeFn) polyhedra. Evidence of a new correlation between the isomer shift and the inductive effect of the competing bond TX (→ Fe)(where X is O or F and T any element with a formal positive charge), J. Phys. Chem. Solids 46 (7) (1985) 763–789, https://doi.org/10.1016/0022-3697(85)90001-0.

[43] E. Tronc, A. Ezzir, R. Cherkaoui, C. Chanéac, M. Noguès, H. Kachkachi, D. Fiorani, A. Testa, J. Greneche, J. Jolivet, Surface-related properties of γ -Fe$_2$ O$_3$ nanoparticles, J. Magn. Magn. Mater. 221 (1-2) (2000) 63–79, https://doi.org/10.1016/S0304-8853(00)00369-3.

[44] D. Kotsikau, V. Pankov, E. Petrova, V. Natarov, D. Filimonov, K. Pokholok, Structural, magnetic and hyperfine characterization of Zn$_x$ Fe$_{3-x}$ O$_4$ nanoparticles prepared by sol-gel approach via inorganic precursors, J. Phys. Chem. Solids 114 (2018) 64–70, https://doi.org/10.1016/j.jpcs.2017.11.004.

[45] A. Pavlenko, K. Zhidel, S. Kubrin, T. Kolesnikova, High-temperature 0.5BiFeO$_3$ –0.5PbFe$_{0.5}$ Nb$_{0.5}$ O$_3$ multiferroic: microstructure, ferroelectric properties, and mössbauer effect, Ceram. Int. 47 (15) (2021) 21167–21174, https://doi.org/10.1016/j.ceramint.2021.04.120.

[46] N. Kalanda, M. Yarmolich, A. Petrov, I. Raevski, S. Kubrin, S. Raevskaya, I. Bobrikov, A. Lazavenka, D.-H. Kim, The influence of cation ordering and oxygen nonstoichiometry on magnetic properties of Sr$_2$ FeMoO$_{6-x}$ around Curie temperature, J. Magn. Magn. Mater. 500 (2020) 166386, https://doi.org/10.1016/j.jmmm.2019.166386.

[47] I. Shivaraja, S. Matteppanavar, P. Krishna, S. Rayaprol, P. Babu, S. Kubrin, B. Angadi, et al., Weak ferromagnetism and magnetoelectric coupling through the spin–lattice coupling in (1- x)Pb(Fe$_{2/3}$ W$_{1/3}$)O$_3$ –(x)BiFeO$_3$ (x= 0.1 and 0.4) solid solution, J. Phys.: Condens. Matter 32 (42) (2020) 425805, https://doi.org/10.1088/1361-648X/aba1aa.

[48] W. Cook, M. Manley, Raman characterization of α -and β -LiFe$_5$ O$_8$ prepared through a solid-state reaction pathway, J. Solid State Chem. 183 (2) (2010) 322–326, https://doi.org/10.1016/j.jssc.2009.11.011.

[49] R.D. Shannon, Revised effective ionic radii and systematic studies of interatomic distances in halides and chalcogenides, Acta Cryst. A 32 (5) (1976) 751–767, https://doi.org/10.1107/s0567739476001551.

[50] K. Mukai, Reversible movement of Zn^{2+} ions with zero-strain characteristic: clarifying the reaction mechanism of Li$_2$ ZnTi$_3$ O$_8$, Inorg. Chem. 58 (15) (2019) 10377–10389, https://doi.org/10.1021/acs.inorgchem.9b01565.

[51] S. Krupička, P. Novák, Handbook of ferromagnetic materials, Vol. 3, North-Holland Publishing Company, 1982, pp. 189–304 (Ch. Oxide spinels).